



City Research Online

City, University of London Institutional Repository

Citation: Koukouvinis, P., Naseri, H. & Gavaises, M. (2017). Performance of turbulence and cavitation models in prediction of incipient and developed cavitation. *International Journal of Engine Research*, 18(4), pp. 333-350. doi: 10.1177/1468087416658604

This is the accepted version of the paper.

This version of the publication may differ from the final published version.

Permanent repository link: <https://openaccess.city.ac.uk/id/eprint/16670/>

Link to published version: <https://doi.org/10.1177/1468087416658604>

Copyright: City Research Online aims to make research outputs of City, University of London available to a wider audience. Copyright and Moral Rights remain with the author(s) and/or copyright holders. URLs from City Research Online may be freely distributed and linked to.

Reuse: Copies of full items can be used for personal research or study, educational, or not-for-profit purposes without prior permission or charge. Provided that the authors, title and full bibliographic details are credited, a hyperlink and/or URL is given for the original metadata page and the content is not changed in any way.

City Research Online:

<http://openaccess.city.ac.uk/>

publications@city.ac.uk

1 Performance of Turbulence and Cavitation Models in

2 Prediction of Incipient and Developed Cavitation

3

4 **Koukouvinis Phoevos***, Naseri Homa and Gavaises Manolis

5 School of Mathematics, Computer Science & Engineering, City University London

6

7 E-mail: Foivos.Koukouvinis.1@city.ac.uk

8

9 **Abstract.** The aim of the current paper is to assess the impact of turbulence and cavitation models on the
10 prediction of Diesel injector nozzle flow. Two nozzles are examined, an enlarged one, operating at incipient
11 cavitation and an industrial injector tip operating at developed cavitation. The turbulence model employed
12 include the RNG $k-\epsilon$, Realizable $k-\epsilon$ and $k-\omega$ SST RANS models, linear pressure-strain Reynolds Stress
13 Model and the WALE Large Eddy Simulation model. The results indicate that all RANS and the Reynolds
14 stresses turbulence models have failed to predict cavitation inception, due to their limitation to resolve
15 adequately the low pressure existing inside vortex cores, which is responsible for cavitation development in this
16 particular flow configuration. Moreover, RANS models failed to predict unsteady cavitation phenomena in the
17 industrial injector. On the other hand, the WALE LES model was able to predict incipient and developed
18 cavitation, while also capturing the shear layer instability, vortex shedding and cavitating vortex formation.
19 Furthermore, the performance of two cavitation methodologies is discussed within the LES framework. In
20 particular, a barotropic model and a mixture model based on the asymptotic Rayleigh-Plesset equation of bubble
21 dynamics have been tested. The results indicate that although the solved equations and phase change formulation
22 is different in these models, the predicted cavitation and flow field were very similar at incipient cavitation
23 conditions. At developed cavitation conditions standard cavitation models may predict unrealistically high liquid
24 tension, so modifications may be essential. It is also concluded that accurate turbulence representation is crucial
25 for cavitation in nozzle flows.

26

27 Keywords: Cavitation, RANS, LES, cavity shedding, step nozzle, Diesel injector

28

29 **1. Introduction**

30 Inception and development of cavitation is a two-way interaction problem between the formed bubbles
31 and the flow. This interaction is enhanced by the fact that most practical flows are turbulent; under
32 such flow conditions the scales of fluid motion underlying in the flow field in the form of vortices can
33 contribute and even become the dominant mechanism causing cavitation formation, leading to
34 structures termed as cavitating vortices¹. Cavitating vortices are common in engineering applications
35 and can exist in propeller blade tip and surfaces, injectors, and pumps. They can significantly affect
36 the flow field characteristics and cause substantial reduction in efficiency and increase erosion. Vortex
37 or string-type cavitation has been observed in studies of in-nozzle flow of Diesel injectors; vortices
38 initiate from the transient flow inside the sac volume and can induce significant hole to hole variations
39 ^{2,3}. Formation of vapour in the core of vortices is an additional mechanism for generation of vorticity,
40 hence it modifies the dynamics of turbulence⁴. Production of vorticity is due to variations in the
41 density which are not aligned with pressure variations and create a baroclinic torque⁵. Experimental
42 studies on stationary hydrofoils shows that baroclinic torques contribute to vorticity generation
43 especially at regions of cavity collapse⁶. Investigation of vorticity generation transport equation shows
44 that vortex stretching, dilatation and baroclinic torque due to density gradients in cavitating flows are
45 major sources of vorticity generation⁷. Cavitating vortices are especially important in erosion studies
46 since they can be very aggressive and cause significant damage as they collapse¹. Erosive vortex rings
47 have been used in industrial applications for cutting rock and underwater cleaning. Numerical
48 comparison of erosive power of a cavitating vortex ring and a spherical bubble indicate that the
49 collapse of cavitating bubble ring should be more erosive than the collapse of a spherical bubble⁸.
50 Vortices are also formed in the shear layer, for example in turbulent wake of bluff bodies, mixing
51 layers of liquid jets or between the recirculation region and bulk flow in separated flows. In a forward-
52 facing-step nozzle, as the flow enters the nozzle and accelerates it separates from the edge, forming a

53 recirculation region at the entrance. The velocity in the recirculation region is lower than the velocity
54 of the bulk flow in the nozzle, hence a shearing layer is formed. These vortices can cavitate and they
55 constantly pair-up forming larger vortices downstream. Shear layer vortices can have small length and
56 time scales and contribute to viscous dissipation⁹. Prediction of this coherent structures of shear flow
57 requires resolving the flowfield down to the inertial subrange.

58 Interaction of turbulence and cavitation has been studied both experimentally and numerically by
59 many researchers on various application fields. In a study with a sharp edged plate in a cavitation
60 channel, Fluorescent Particle Image Velocimetry (PIV) is used to assess the effect of cavitation on
61 shear layer instabilities and flow turbulence downstream the shear layer¹⁰. The two-way interaction
62 between cavitation and turbulence was investigated with Direct Numerical Simulation (DNS) with
63 main interest on the development of shear layer instabilities¹¹. It is reported that turbulence is
64 modulated by cavitation. This modulation can form a basis for a Sub Grid Scale (SGS) model for
65 cavitation in Large Eddy Simulation (LES). Reynolds Averaged Navier-Stokes (RANS) models are
66 computationally less expensive than LES but they can have significant shortcomings in modelling
67 turbulent cavitating flows. It has been shown that traditional RANS/URANS models may overestimate
68 turbulent viscosity in cavitation zones, preventing the development of a re-entrant jet motion and the
69 cavity shedding pattern, yielding unnatural results¹²⁻¹⁴. Eventually, a correction¹⁵ has been applied in
70 order to modify the turbulent kinetic energy term in the two equation model closure by reducing the
71 eddy viscosity in mixture regions and with this term it was possible to replicate the observed
72 experimental shedding pattern. The divergence of the velocity fluctuations is not zero in mixture
73 transport equations of RANS models and additional dissipation terms appear¹⁶. Without including the
74 extra dissipation terms, namely the mixture pressure dilatation, mixture turbulent mass flux and the
75 compressible dissipation, a stable cavity without recirculation and shedding is predicted. By adding
76 the dissipation due to mixture compressibility, the re-entrant jet motion is predicted which results in
77 predicting the cyclic behaviour of cavitation. Other approaches to predict turbulent unsteadiness in

78 cavitating flows include limiting the eddy viscosity by applying a filter-based modification to k- ϵ
79 model¹⁷ or adding a scale-adaptive term to transport equation of the turbulent length scale in k- ℓ
80 turbulence model¹⁸. Other researchers^{3, 19, 20} have tried to compensate for the turbulent effect on
81 cavitation inception through the inclusion of an additional semi-empirical pressure fluctuation term to
82 the saturation pressure. The importance of accurately capturing the turbulence induced pressure
83 fluctuations in cavitating flows is highlighted in a study by Edelbauer et al.²¹, with main focus on
84 throttles and constrictions appearing in fuel injection systems. They have compared RANS and LES
85 simulations of a cavitating throttle flow; even though they have employed a rather specialized variant
86 of the v^2 - f turbulence model, they were unable to get good results in all cases examined, showing the
87 situational applicability of the RANS model. They conclude that RANS can predict cavitation with a
88 reasonably acceptable accuracy in an operating condition with high pressure difference, whereas it
89 fails to predict the cavitation at a lower pressure difference. It is worth mentioning the recent work of
90 Örley et al.²², who employed an LES framework with cut-cell immersed boundary method and a
91 barotropic fluid, including the effect of non-condensable gas, for the simulation of a 9-hole Diesel
92 injector to obtain time resolved information on cavitating/turbulent flow structures in the injector sac,
93 orifices and jets.

94 The aim of the present work is to examine the influence of various turbulence models, including some
95 common RANS models e.g. k- ϵ , k- ω , RSM, as well as some of their modifications that have been
96 proposed for the compensation of mixture compressibility effects, such as the Reboud *et al.* correction
97¹⁵. The application is on a square throttle with a sudden constriction which has been examined in the
98 past both experimentally and numerically²³; this configuration bears resemblance to the constrictions
99 inside injector passages. The results indicate that traditional turbulence models and even their
100 modifications fail to predict the incipient cavitation formation due to shear layer instabilities. Further
101 application in the flow of a Diesel injector tip suggests that while RANS models predict cavitation
102 formation, the formed cavity may be unphysically stable, especially when hole tapering is present.

103 However, more advanced turbulence models, such as Wall Adapting Local Eddy-viscosity²⁴ (WALE)
104 LES are found to capture cavitation inception and development. Cavitation effects have been be
105 modelled using a mixture model, where phase change is governed by the Schnerr and Sauer²⁵ and
106 Zwart *et al.*²⁶ models. In addition, a new formulation of a Homogenous Equilibrium Model (HEM),
107 similar to that developed by Schmidt²⁷, has been utilized.

108 **2. Mathematical modelling of turbulence and cavitation**

109 In this section, a brief description of the mathematical background of the involved models will be
110 described, both regarding turbulence models and cavitation modelling. All the relevant models
111 discussed have been employed using the ANSYS Fluent v15 software, either in the form of pre-
112 existing models, or as programmed modifications through User Defined Functions (UDFs).

113 Since high accuracy is necessary to resolve fine features of flow, such as the vortex interaction with
114 cavitation, second order schemes have been used for resolving the momentum equations, in case of
115 RANS models. For the WALE LES model, a blended central/second order upwind scheme has been
116 used for the momentum equation, since it is a good compromise between stability and low numerical
117 diffusion. The density field was discretized with a second order upwind scheme, whereas the phase
118 field in the 2-phase model was discretized with the Quadratic Upstream Interpolation for Convective
119 Kinetics (QUICK) scheme in order to capture the high density ratios. Time advancement is done with
120 a second order implicit method (three time level predictor-corrector, or midpoint method), to maintain
121 accuracy and remove any time stepping stability constraints.

122 *2.1. Turbulence modelling*

123 Turbulence is an effect associated with chaotic and unsteady nature of fluid motion at high Reynolds
124 numbers; indeed at such cases a complicated flow pattern emerges with many temporal and spatial
125 scales of fluid motion, manifested as vortices through which an energy transfer occurs, from the
126 largest scales of fluid motion to the smallest scales, where energy is dissipated due to viscous effects

127 ²⁸. The fundamental problem with turbulence is the fact that DNS of all scales is impossible for most
128 industrial flows. The alternative is to emulate the effect of the energy transfer process with a proper
129 model. This has the advantage that it is no longer required to take into account all relevant scales of
130 fluid motion, but rather consider only the largest ones, depending on the model used. For example,
131 RANS models focus only on the mean flow properties, whereas Large Eddy Simulation models
132 include also the effect of the larger eddies which are anisotropic and model only the smallest ones; this
133 fact forces the simulation in the latter option to be always in 3D and transient.

134 In the current work several well-known RANS models have been employed. These are the RNG k- ϵ ,
135 Realizable k- ϵ , SST k- ω and Reynolds Stress models. Some brief characteristics of these models are
136 given below and the interested reader is addressed to a CFD handbook reference for more information,
137 e.g. ²⁸⁻³⁰:

138 - The k- ϵ model family is a 2-equation turbulence model, where the turbulent kinetic energy (k) and
139 the turbulence dissipation (ϵ) are modelled using transport equations with diffusion and source terms
140 calibrated from experiments. It is one of the most widely used models in industrial cases. Its main
141 deficiency is the overestimation of turbulence production at stagnation points and underestimation of
142 separation in adverse pressure gradients. Over time, modifications as the RNG and Realizable k- ϵ
143 models have been developed to improve the accuracy of the model.

144 - The k- ω model family is a 2-equation turbulence model as well, which solves for turbulent kinetic
145 energy (k) and specific dissipation rate (ω); this gives several advantages in respect to the k- ϵ model in
146 predicting near wall regions accurately, due to the nature of the ω -equation in respect to the ϵ -
147 equation. However, the standard k- ω model is somewhat sensitive to the boundary conditions of the
148 specific dissipation rate. For that reason, the k- ω Shear Stress Transport (SST) model was developed,
149 which is a blend between the k- ϵ and k- ω models, offering the best of both models.

150 - The linear strain pressure-strain Reynolds Stress Model (RSM), based on the work of Launder³¹, is a
 151 more advanced version of the RANS models, which no longer assumes isotropy of the Reynolds
 152 stresses; contrary, one equation for each Reynolds stress term is solved, in addition to the turbulence
 153 dissipation. Eventually this leads to seven additional equations for 3D, which adds to a significant
 154 computational cost, but potentially it is the most general of the RANS models.

155 Additionally to the aforementioned models, the Reboud *et al.* modification¹⁵ shall be examined; this
 156 modification aims to compensate the effect of the mixture compressibility in the vapour/liquid mixture
 157 region³². In general, the correction is applied during the calculation turbulent viscosity, where density
 158 ρ is replaced with a function $f(\rho)$, as follows:

$$159 \quad f(\rho) = \rho_V + (1 - \alpha)^n (\rho_L - \rho_V) \quad (1)$$

160 where ρ is density, V and L indexes correspond to saturated vapour and liquid density respectively and
 161 n is an exponent the takes values ~ 10 .

162 Eventually turbulent viscosity has the form¹²:

$$163 \quad \mu_t = C_\mu f(\rho) \frac{k^2}{\varepsilon} \quad (2)$$

164 for the RNG k- ε model, or for the k- ω SST model:

$$165 \quad \mu_t = f(\rho) \frac{a_1 k}{\max(a_1 \omega, S F_2)} \quad (3)$$

166 where $C_\mu = 0.845$, $a_1 = 5/9$, $S = \sqrt{2S_{ij} : S_{ij}}$ with S_{ij} the components of the rate of strain tensor and F_2 a
 167 blending function³⁰. These corrections are relevant only in unsteady simulations (URANS). Moreover,
 168 when compressible flow is involved, such as in the Diesel injector or the barotropic HEM model, an
 169 additional turbulence dissipation term is included in the turbulent kinetic energy equation, based on
 170 the modification of Sarkar *et al.*³³.

171 Apart from the aforementioned RANS models, the Wall Adapting Local Eddy-viscosity (WALE)
172 model has been employed for the LES runs, since it is known that it performs significantly better in
173 the near wall region in respect to the basic Smagorinsky LES model ²⁴.

174 2.2. Cavitation modelling: the barotropic Homogenous Equilibrium Model (HEM)

175 For the homogenous equilibrium model, additional phase field variables are not needed, since the mass
176 transfer occurs instantaneously, linking pressure to density only. So, one needs an appropriate equation
177 of state (EOS) that corresponds to the phase change of the liquid to the liquid/vapour mixture.

178 In this work, for simplicity the influence of thermal effects have been omitted and a barotropic EOS is
179 constructed as follows:

180 - the Tait EOS is used for the liquid, i.e. when $\rho \geq \rho_l$

181 - the isentropic gas EOS is used for the gas, i.e. when $\rho_v > \rho$

182 - for the mixture ($\rho_l > \rho \geq \rho_v$), the EOS is based on the Wallis speed of sound formula ³⁴:

$$183 \quad \frac{1}{c_m^2 \rho_m} = \frac{a_l}{c_l^2 \rho_l} + \frac{a_v}{c_v^2 \rho_v} \quad (4)$$

184 where a corresponds to volume fraction, c to the speed of sound, ρ to the density and l and v indexes to
185 liquid and vapour respectively. Considering that, for an isentropic fluid the speed of sound is ³⁵:

$$186 \quad c^2 = \left(\frac{\partial p}{\partial \rho} \right)_s \quad (5)$$

187 it is possible to integrate eq. 5 in respect to the mixture density and obtain pressure (see also appendix
188 A). Eventually, the complete equation of state is the following, see also an indicative graph of the EOS
189 at Figure 1:

$$190 \quad p(\rho) = \begin{cases} B \left[\left(\frac{\rho}{\rho_l} \right)^n - 1 \right] + p_{sat,L} & \rho \geq \rho_l \\ \frac{c_v^2 c_l^2 \rho_l \rho_v (\rho_v - \rho_l)}{c_v^2 \rho_v^2 - c_l^2 \rho_l^2} \ln \left(\frac{\rho}{c_l^2 \rho_l (\rho_l - \rho) + c_v^2 \rho_v (\rho - \rho_v)} \right) + p_{ref} & \rho_l \geq \rho > \rho_v \\ C \rho^\gamma & \rho_v > \rho \end{cases} \quad (6)$$

191 The factor B corresponds to the bulk modulus of the liquid, n is an exponent determining the stiffness
192 of the Tait equation of state, which is commonly set to 7.15 for weakly compressible liquids³⁶, C is
193 the constant of the isentropic process and γ is the heat capacity ratio. In the above equation p_{ref} and
194 $p_{sat,L}$ are reference values in order to make sure that the pressure is a continuous function of density,
195 thus $\lim_{\rho \rightarrow \rho_v^+} p(\rho) = \lim_{\rho \rightarrow \rho_v^-} p(\rho)$ and $\lim_{\rho \rightarrow \rho_l^+} p(\rho) = \lim_{\rho \rightarrow \rho_l^-} p(\rho)$. It becomes obvious from the formulation of the
196 equation, that during the phase change there is a small pressure difference equal to $\Delta p = p_{sat,L} - p_{sat,V}$.
197 In practice, this difference is small in comparison with the pressure levels involved in the simulation,
198 e.g. for the present case, the difference is around 4500Pa, whereas the pressure level in the current
199 simulation is of the order of ~2bar. Moreover, while it is true that the equation of state is not perfectly
200 accurate for the sharp change of pressure in the saturation dome, it has the advantage of having a
201 continuous speed of sound, which helps achieving convergence with the pressure-based solver
202 utilized. The values used in this study are shown in Table I.

203 Table I. Thermodynamic properties for water/vapour with the barotropic HEM, values have been
204 selected an saturation properties of water/steam at 20°C³⁷.

Liquid properties			Vapour properties		
B	307.1·10 ⁶	Pa	C	27234.7	Pa/(kg/m ³) ^γ
n	7.15	(-)	γ	1.33	(-)
$\rho_{sat,L}$	998.16	kg/m ³	$\rho_{sat,V}$	0.0171	kg/m ³
$c_{sat,L}$	1483	m/s	$c_{sat,V}$	97.9	m/s
$p_{sat,L}$	4664.4	Pa	$p_{sat,V}$	125	Pa
μ_L	10 ⁻³	Pa.s	μ_V	9.75·10 ⁻⁶	Pa.s

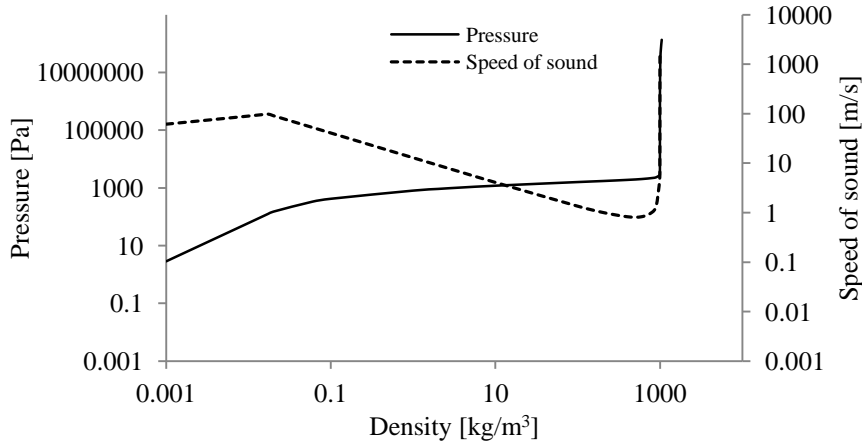


Figure 1. A graph showing the behaviour of the barotropic HEM EOS and the speed of sound variation.

2.3. Cavitation modelling: the two phase mixture model

The two phase mixture model, assumes mechanical equilibrium between the two phases, i.e. both liquid and vapour phase share the same pressure and velocity fields. An additional advection equation corresponding to the vapour fraction is solved, in the following form:

$$\frac{\partial(a\rho_v)}{\partial t} + \nabla(a\rho_v\mathbf{u}) = R_e - R_c \quad (7)$$

where a is the vapour fraction, ρ_v is the vapour density, \mathbf{u} is the velocity field and R_e , R_c are the mass transfer rates for condensation (c) and evaporation (e). These terms are commonly associated with semi-empirical bubble dynamic models, based on the simplified, asymptotic Rayleigh-Plesset equation, but include additional user calibrated terms; two commonly used models, that will be examined in this study are the Zwart-Gerber-Belamri (ZGB)²⁶ and Schnerr-Sauer (SS) models²⁵. In fact, the two phase model could be treated as a non-thermodynamic equilibrium model and an increase of the mass transfer rates R_e and R_c towards infinity will push the model towards thermodynamic equilibrium. Thus, for low mass transfer rates, it is not uncommon to observe regions of negative pressures. While negative pressures, or tension, has been found in delicate experiments in liquids (for

222 example ^{1, 34, 38}), one could question the existence of such cases in industrial scenarios. Especially for
 223 water in cavitation tunnels there is evidence that pressure at the cavitation region matches closely the
 224 saturation pressure at the given temperature ³⁹. So, in practice, one may have to tune the mass transfer
 225 terms in order to prevent as much as possible the existence of negative pressure zones.

226 For applying the two phase model, one needs to specify the properties and equation of state for the
 227 different materials. For the liquid phase either the incompressible assumption or the Tait equation of
 228 state is used. On the other hand, the gas/vapour phase is assumed to be incompressible. It must be
 229 highlighted here that even if the pure vapour phase is incompressible, the mixture is not, since mass
 230 transfer is involved; actually, the mass transfer is the dominant term affecting mixture compressibility
 231 ¹. The properties used for the materials involved are summarized in the following table; for the
 232 incompressible liquid, bulk modulus B and speed of sound c are no longer applicable.

233 Table II. Thermodynamic properties for water/vapour with the 2-phase model, values have been
 234 selected an saturation properties of water/steam at 20°C ³⁷.

Liquid properties			Vapour properties		
B	$307.1 \cdot 10^6$	Pa	$\rho_{sat,V}$	0.0171	kg/m ³
n	7.15	(-)	μ_V	$9.75 \cdot 10^{-6}$	Pa.s
$\rho_{sat,L}$	998.16	kg/m ³			
$c_{sat,L}$	1483	m/s			
$p_{sat,L}$	2340	Pa			
μ_L	10^{-3}	Pa.s			

236

237

238 3. Square Throttle Case and Simulation Setup

239 The experimental setup is extensively reported in the reference study ²³, so the operating conditions
 240 and geometry are only briefly presented here. Water is discharged into a rectangular step nozzle with
 241 48 ml/s flow rate and the outlet is subjected to atmospheric pressure. At these conditions a

242 recirculation region forms downstream the sharp step constriction and cavitation develops at the shear
243 layer between the recirculation zone and the formed jet ²³.

244 The dimensions of the constriction are 1.94x1.94x8mm (W×H×L) and the schematic of the nozzle is
245 shown in Figure 2a along with velocity measurement positions. It should be noted that in the
246 simulations the outlet is not placed directly at the end of the throttle, but rather further downstream in
247 order to minimise its interference to the flow pattern developing in the throttle (see Figure 2b). The
248 average velocity through the nozzle is 12.8m/s and the Reynolds number is Re=27000; these
249 conditions correspond to incipient cavitation with cavitation number:

$$250 \quad \sigma = \frac{p_{amb} - p_{vap}}{\frac{1}{2}\rho u^2} = 1.2 \quad (8)$$

251 where p_{amb} is the ambient pressure (atmospheric), p_{vap} is the vapour pressure, ρ the liquid density and u
252 the characteristic velocity. Also, for the sake of completeness, we provide the value of an alternative
253 definition for the cavitation number, denoted as CN , equal to $1/\sigma$; for the specific case $CN=0.83$. Based
254 on these characteristics it is possible to make an estimate of the Kolmogorov scales and Taylor
255 microscale of fluid motion for this case ²⁹:

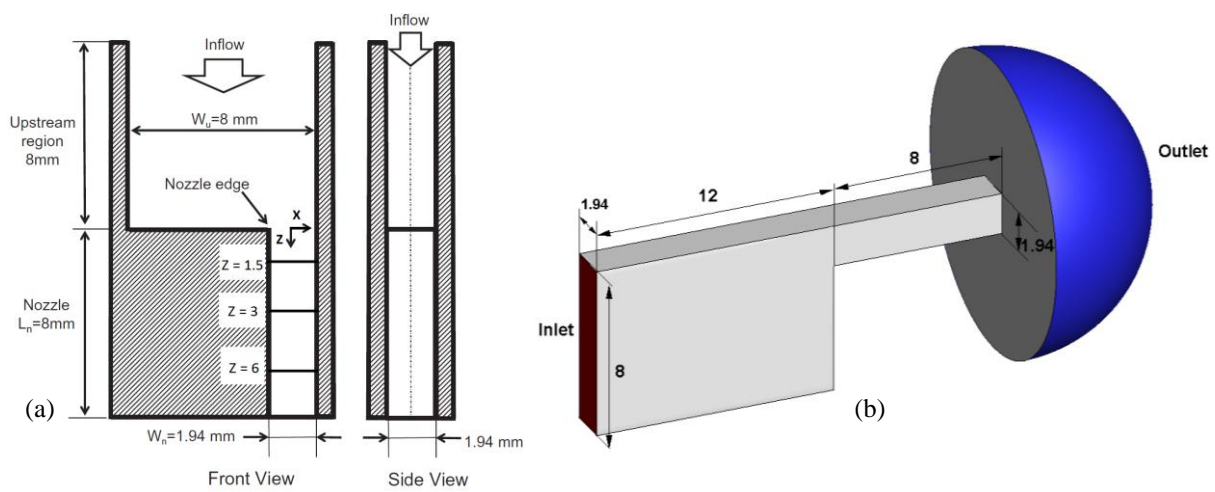
$$256 \quad \text{Kolmogorov length scale } \eta = \left(\frac{\nu^3}{\varepsilon} \right)^{1/4} = 0.98 \mu m \quad (9)$$

$$257 \quad \text{Kolmogorov time scale } \tau_\eta = \left(\frac{\nu}{\varepsilon} \right)^{1/2} = 0.96 \mu s \quad (10)$$

$$258 \quad \text{Taylor length scale } \lambda_g = \sqrt{10} \text{Re}^{-0.5} L = 39 \mu m \quad (11)$$

259 where ν is the kinematic viscosity which is $\sim 10^{-6} \text{m}^2/\text{s}$ for water, ε is the turbulent dissipation, estimated
260 roughly as u^3/L , with u a characteristic velocity, e.g. 12.8m/s, and L a characteristic length scale, e.g.
261 1.94mm. For the LES studies, as an initial guideline for the mesh sizing we have used a common

262 practice in the relevant literature, suggesting a grid size of the order of the Taylor length scale, since it
 263 lies at the dissipation region end of the inertial subrange; this mainly applies for isotropic turbulence,
 264 so it is used as a rough estimate for the mesh generation. It must be stressed that apart from this
 265 practical guideline, the turbulent kinetic energy spectrum was examined, in order to make sure that it
 266 obeys the $-5/3$ law for the energy cascade, see Pope²⁹. The interested reader is addressed to several
 267 references⁴⁰⁻⁴² discussing on the subject of grid sizing in LES for practical flows.



268
 269 Figure 2. (a) Nozzle geometry²³ and (b) the computational domain used, with the boundary conditions shown;
 270 red corresponds to inlet, grey to walls and blue to outlet. All dimensions are in mm.

271
 272 The simulations to be presented are detailed as follows:

273 1. First of all a grid dependence study was conducted with meshes of three different resolutions. These
 274 cases have been examined as single phase, for simplicity, and in steady state and imposed flow rate of
 275 48ml/s. From these, the optimum resolution was determined for further examination with the rest
 276 RANS cases. Additionally, the total pressure at the inlet of the throttle for the given flow rate was
 277 determined and used as a convergence criterion for the grid dependence study and as a boundary
 278 condition for the rest of the simulations.

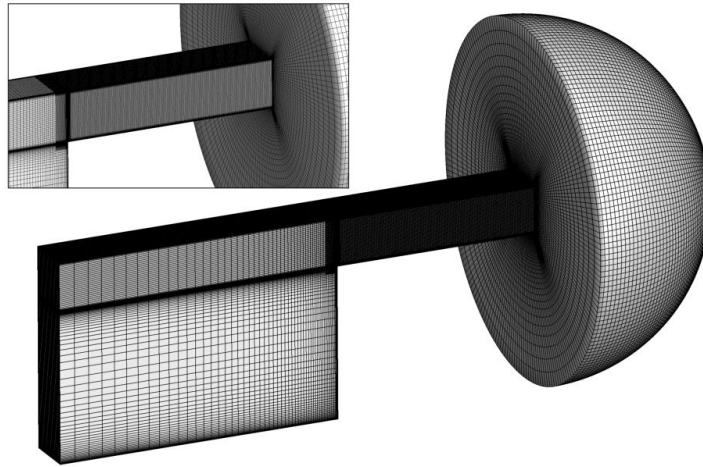
279 2. Then, the influence of the RANS models is examined. The models investigated are the Realizable k-
280 ϵ , k- ω SST and the RSM. Again, these cases are examined under steady state.

281 3. The modified RNG k- ϵ and k- ω SST models have been further examined, with the Reboud *et al.*
282 correction¹⁵. Since the improvement of this correction is related to the prediction of cavity shedding
283 process, these cases are treated as unsteady.

284 4. The WALE LES model²⁴ is examined with various cavitation models, such as the Zwart-Gerber-
285 Belamri, Schnerr-Sauer, Barotropic HEM and tuned Zwart-Gerber-Belamri. Due to the nature of the
286 LES model, these cases are treated as unsteady too.

287 In all simulations at steps 2, 3 and 4, total pressure is imposed at the inlet, which is determined from
288 step 1, and static pressure at the outlet. This combination works better for the transient cases, where
289 partial blockage might be induced due to cavitation shedding and this might cause unrealistic pressure
290 build-up at the inlet, should a fixed flow rate be imposed.

291 The computational mesh employed in all cases is block-structured. Mesh refinement with inflation
292 layers, is employed in critical areas, such as in the vicinity of the walls. The average mesh resolution
293 for the grid dependence study is 90 μm , 75 μm and 50 μm , corresponding to 1M, 2.4M and 6.8M cells.
294 The temporal resolution for the unsteady RANS is 1 μs . For the LES mesh a similar mesh was used,
295 with telescopic refinement to achieve high resolution in the area of interest (see Figure 3). The LES
296 cell count is ~4M cells, but the spatial resolution is 20 μm in the core of the throttle, while there is
297 refinement towards the walls; the spatial resolution chosen is less than the Taylor length scale, based
298 on practical guidelines. Given that an average velocity of ~12m/s occurs inside the throttle, a relevant
299 time scale is 2 μs . The time step size chosen is 1 μs , which corresponds to a CFL number of 0.5, enough
300 to properly describe the time scales of fluid motion. Based on the LES simulation results, y^+ varies
301 around 0.2-1 in the throttle. The near wall resolution is ~2.5 μm , resulting to 6-7 cells within the
302 viscous sublayer, which has a thickness of $\delta_s = 5 \cdot \nu / u_* \sim 15\mu\text{m}$ ²⁹.



303
304 Figure 3. The LES mesh. The block-structured topology of the mesh is visible, as well as the telescopic
305 refinement near the throttle entrance.

306 In all cases, the interest is on the average velocity distribution and RMS of velocity fluctuations in
307 locations for which experimental measurements exist ²³, i.e. at 1.5, 3 and 6mm downstream the edge
308 of the throttle. It should be noted that since experimental data have been collected on the midplane of
309 the geometry using Laser Doppler Velocimetry, this limits the information of the average velocity and
310 RMS velocity fluctuations only to the x and z velocity components, see also the Front view, Figure 2.

311 Averaged fields are provided by steady state RANS by default, whereas RMS of velocity fluctuations
312 are determined through total turbulent kinetic energy under the Boussinesq relationship for 2- ϵ -
313 models ²⁸, or directly from the computed Reynolds stresses, when the RSM model is used. For
314 transient runs, such as LES, the time history of all velocity components is recorded and then the
315 relevant components are used for comparisons. Qualitative comparisons of the cavitation pattern
316 inside the throttle is examined when applicable.

317 **4. Numerical results and comparison with experiments**

318 *4.1. Grid dependency test*

319 As mentioned in the previous section, three different grid spacings have been tested to assess the
320 sensitivity of the results on the mesh resolution. In this section the results will be presented for the $k-\omega$

321 SST model; similar results have been obtained for other turbulence models. Grid dependency test
322 results are reported in table III along with effect of grids on the total pressure at inlet. The calculated
323 total pressure at inlet is affected less than 0.5%, giving confidence to use it as a boundary condition
324 for the rest of the simulations. Moreover, all resolutions give a velocity distribution very similar to the
325 experimental profile and the difference between subsequent refinements is not significant.

326 Table III. Grid parameters and their effect on total pressure at inlet.

Grid	Cells	Max y^+	Min y^+	Total pressure at inlet [Pa]
Coarse	1M	55	1	237260
Medium	2.3M	45	0.5	238270
Fine	6.8M	37	0.2	238220

327
328 Given the aforementioned results, the medium resolution is selected for the rest RANS studies, since it
329 succeeds in capturing a velocity distribution very close to the experiment, while it does not predict a
330 significantly different total pressure from the finest resolution employed.

331 4.2. Standard RANS models results

332 In this section the results from steady state RANS simulations will be discussed. All RANS models
333 give an adequate prediction of the velocity distribution compared to experimental measurements of
334 velocity inside the nozzle²³. However, all the examined models fail to predict accurately the turbulent
335 fluctuations near the nozzle exit at $z = 6\text{mm}$ (see figure 2(a)). These discrepancies can be attributed to
336 the steady state assumption of the flow and failure of all standard RANS models to predict cavitation.

337 Indeed, a very important observation, and an important conclusion of the present study, is that the
338 steady state RANS models examined so far, fail to predict the onset of cavitation. To be more precise,
339 the minimum pressure in the whole computational domain predicted by the models, as described so
340 far, is:

341 - for the Realizable k- ϵ , 12970Pa

342 - for the k- ω SST, 10590Pa

343 - for the RSM, 13770Pa

344 It becomes clear that these minimum pressures are almost 5-6 times the saturation pressure of water,
345 so cavitation is not predicted; in fact even applying corrections that increase the cavitation threshold
346 pressure due to the influence of turbulence fluctuations (see e.g. ²⁰) still fail to produce cavitation.

347 Assuming a cavitation threshold of the form:

$$348 \quad p_v = p_{sat} + \frac{1}{2}(0.39k\rho) \quad (12)$$

349 where p_{sat} the saturation pressure, k the local turbulent kinetic energy and ρ the liquid density, the
350 maximum threshold pressure for cavitation formation throughout the whole computational domain is:

351 - for the Realizable k- ϵ , 6515Pa

352 - for the k- ω SST, 7128Pa

353 - for the RSM, 8047Pa

354 which is still significantly lower, almost half, of the minimum liquid pressure that has been predicted
355 in the computational domain by each model.

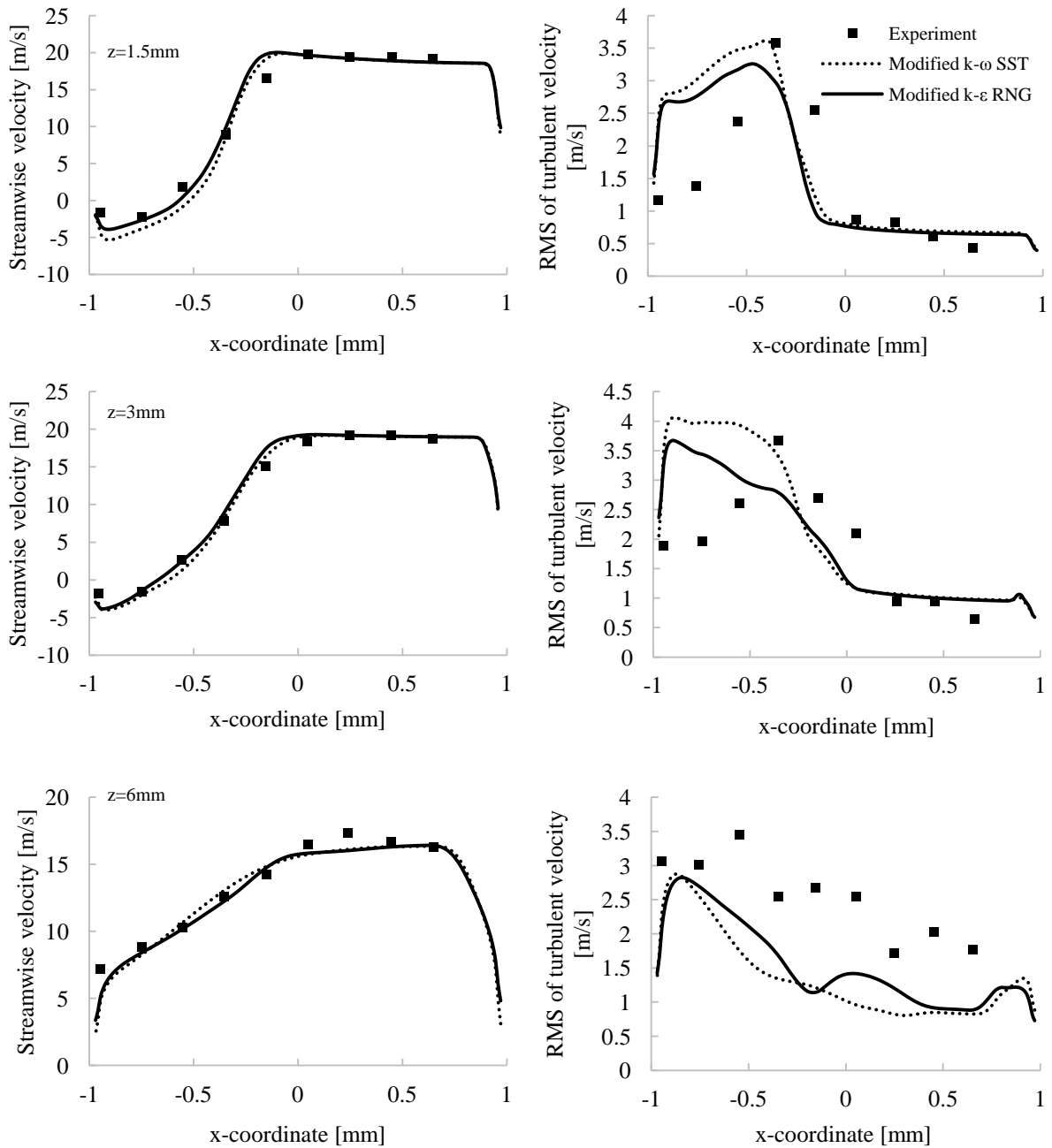
356

357 *4.3. Modified URANS models results*

358 Since it is suspected that part of the discrepancies is due to the steady state assumption of the flow,
359 further examination of the case with unsteady RANS models has been conducted. Additionally, since
360 it is known from the experiment that cavitation shedding occurs, due to the shear layer instabilities at
361 the border of the recirculation zone, it was chosen to resort to the RANS modifications described in
362 section 2.3, which are known to be able to predict such effects.

363 As shown in Figure 4, comparison between the modified URANS models and experimental data
364 shows a close match in streamwise velocity profiles. It is notable that the velocity distribution matches
365 closely to the experimental data at all locations $z = 1.5, 3$ and 6 mm. The same observation applies for

366 the RMS of turbulent velocity fluctuation as well; note that the turbulent distribution has the correct
 367 pattern at the location of $z = 6\text{mm}$, even though it is slightly underestimated.



368

369

370

371 Figure 4. Streamwise velocity distribution and RMS of turbulent velocity at different locations downstream the

372 throttle edge, for different modified URANS models. The experimental results are indicated with squares.

373

374 A very important observation here is that still the unsteady RANS simulations failed to predict
375 cavitation formation, even though flow unsteadiness has been observed. Since the nature of the
376 correction is the reduction of turbulent viscosity in the mixture region, while reverting to the standard
377 URANS formalism in the pure liquid/vapour phases, it is reasonable to conclude that the correction
378 was not applied at all. To force the correction to operate, an amount of vapour was artificially
379 introduced inside the recirculation region, in the centre of the large scale vortex, where pressure was
380 lower, hoping that this would trigger cavity shedding. Unfortunately, even if unsteadiness temporarily
381 was enhanced, after several time steps cavitation structures eventually collapsed, returning to the prior
382 condition of pure liquid.

383

384 *4.4. LES WALE results*

385

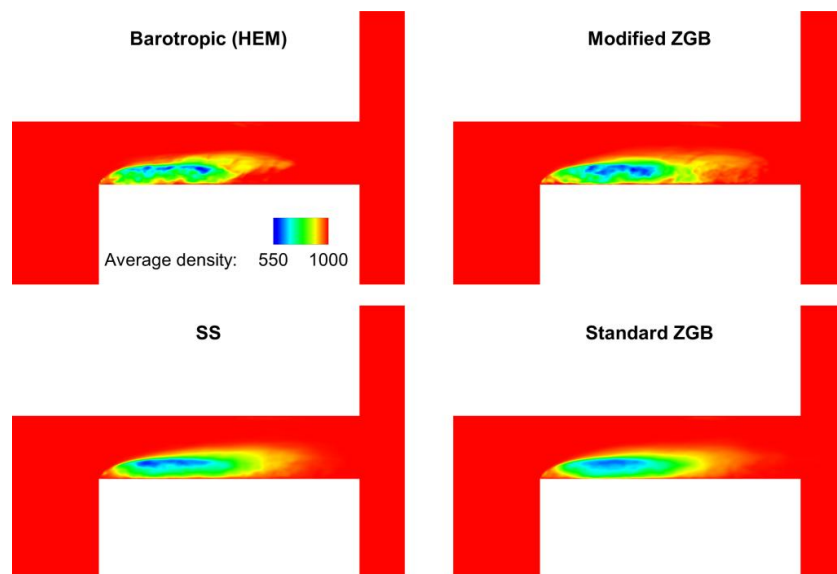
386 The last results to be presented refer to the WALE LES model. In Figure 6 average velocity and RMS
387 velocity fluctuations are shown, as before.

388 It is of interest that LES succeeds in predicting accurately the velocity distribution at all locations and
389 provides very good estimates of the turbulent fluctuations both at the recirculation zone and the jet
390 formed at the core of the throttle. Moreover cavitation is predicted with all cavitation models,
391 predicting a very similar velocity profile, showing that the velocity distribution is rather weakly
392 related to cavitation presence; this is explained by the low cavitation intensity of the examined
393 configuration. The same applies for the average volume fraction distribution, as shown in Figure 5, for
394 the examined models. Statistics were collected for 3000 time steps (or 3ms), thus slight scattering is
395 present. However, the average cavitation development is similar for all cavitation models.

396 Considering the minimum pressures that develop inside the computational domain:

- 397 - The modified coefficient ZGB model, instantaneous minimum $\sim -3000\text{Pa}$ and minimum average
 398 $\sim 7200\text{Pa}$.
- 399 - The barotropic model, instantaneous minimum $\sim 500\text{Pa}$ and minimum average $\sim 9800\text{Pa}$.
- 400 - The standard ZGB model, instantaneous minimum $\sim -12000\text{Pa}$ and minimum average $\sim 7800\text{Pa}$.
- 401 - The standard SS model, instantaneous minimum $\sim -20000\text{Pa}$ and minimum average $\sim 8600\text{Pa}$.

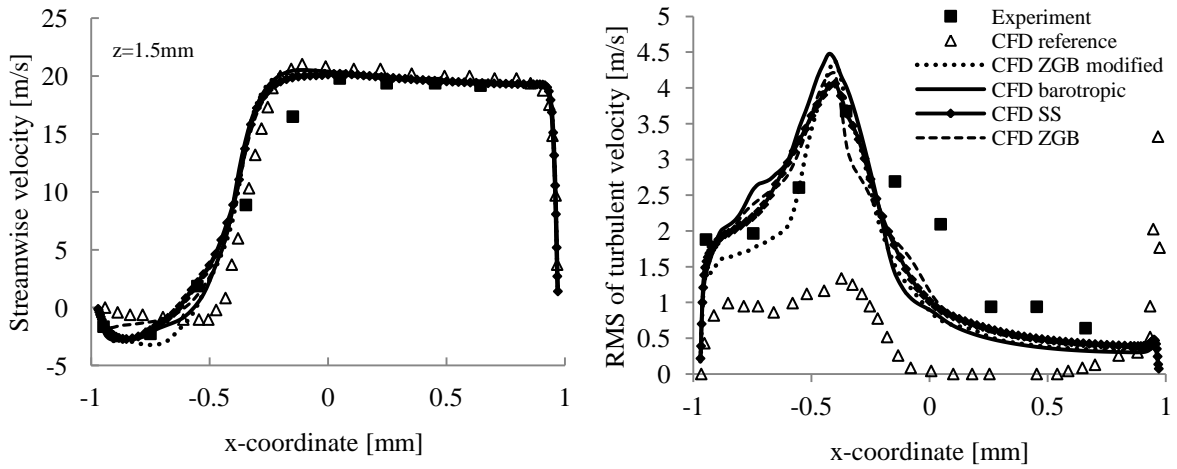
402 The barotropic model is the only one that predicts a positive minimum pressure, due to the
 403 Homogenous Equilibrium assumption; in fact a negative pressure in the barotropic model does not
 404 have any meaning, since it corresponds to negative density and non-real speed of sound, see eq. 6. The
 405 other models, predict negative pressures which drive the mass transfer from liquid to vapour phases.
 406 Indicative flow instances are presented in Figure 7, showing the shedding of cavitation structures, the
 407 highly transient velocity and pressure distributions for the barotropic HEM.



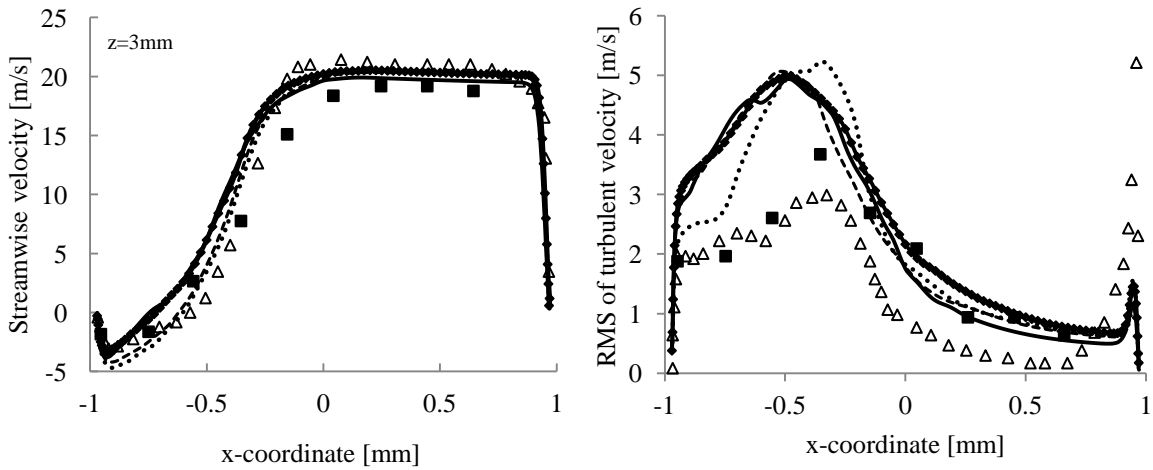
408

409 Figure 5. Indicative average density distribution downstream the constriction with several cavitation models, the
 410 barotropic HEM and the 2-phase modified ZGB, Schnerr Sauer and standard ZGB models. Units are in SI, i.e.
 411 $[\text{kg}/\text{m}^3]$ for density.

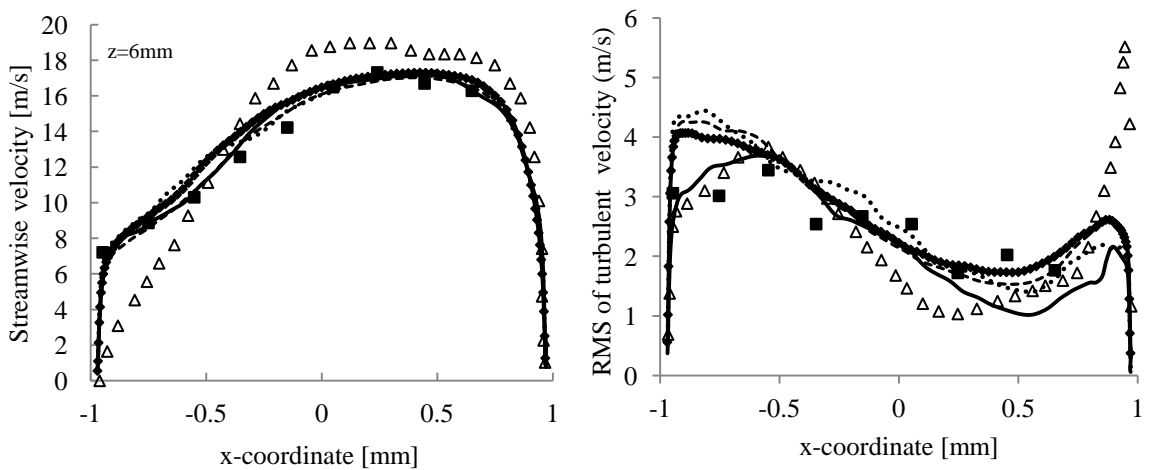
412



413



414



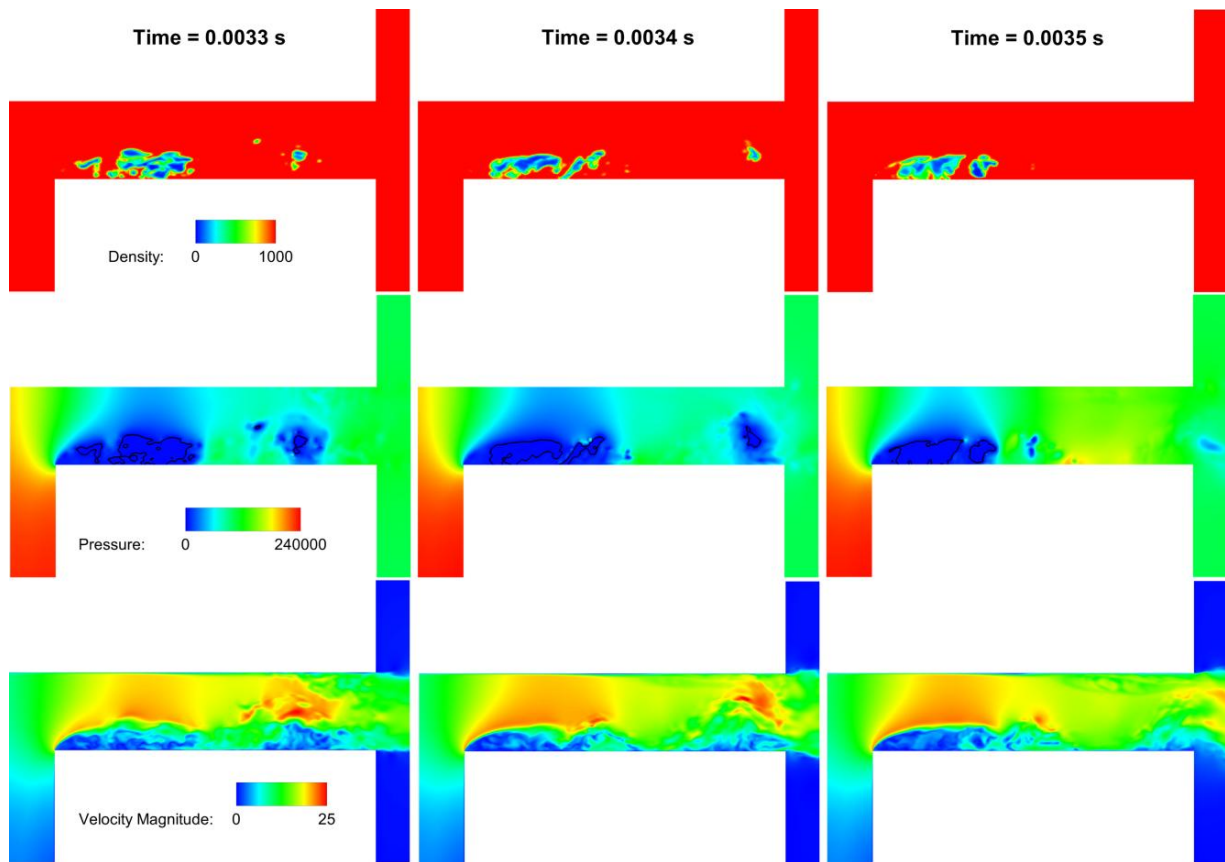
415

416

417

418

Figure 6. Average streamwise velocity distribution and RMS of turbulent velocity at different locations downstream the throttle edge, for LES and with different cavitation models. The experimental results are indicated with squares and the reference CFD results²³ with triangles.



419

420 Figure 7. Barotropic HEM model: Instances of the instantaneous density, pressure field (the black line shows
 421 regions of pressure below saturation pressure) and velocity distribution at 0.1ms intervals. The high flow
 422 unsteadiness is clearly visible. Units are in SI, i.e. $[\text{kg}/\text{m}^3]$ for density, $[\text{Pa}]$ for pressure and $[\text{m}/\text{s}]$ for velocity.

423

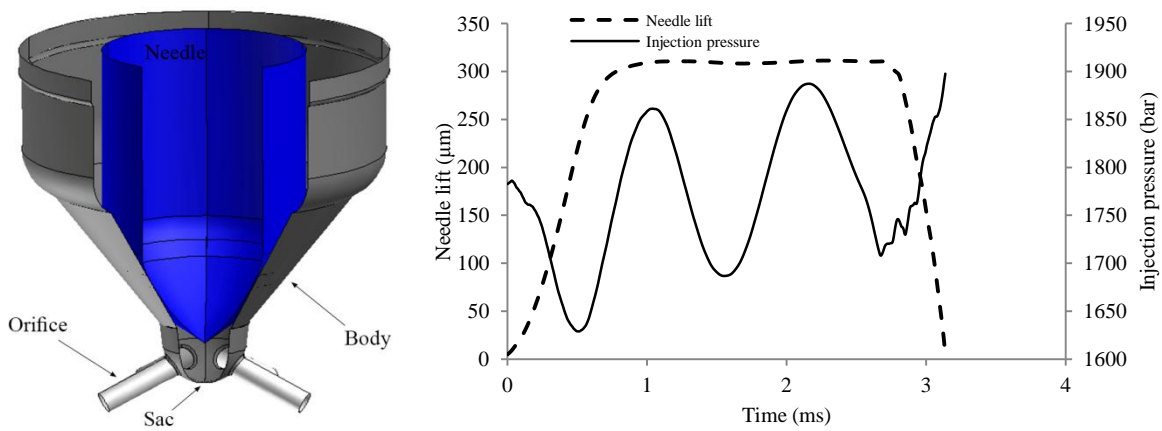
424 It is important to remark that even the LES model employed predicts an average pressure that is higher
 425 than the saturation pressure, in a similar fashion as the RANS simulations. However, instantaneously
 426 pressure inside the vortices formed due to the shear layer instabilities drops below saturation, causing
 427 the formation of highly transient cavitation structures.

428 5. Simulations in Diesel injector

429 In this section, results from the LES simulation of the flow inside a Cat® Diesel injector will be
 430 presented. It has to be kept in mind that a complete Diesel injector is a rather complicated device,
 431 involving the interaction of hydraulic, electrical and mechanical components, for more information the

432 interested reader is addressed to the work of Egler et al.⁴³. The main focus here will be at the tip of the
 433 Diesel injector, as shown in Figure 8, where the main components, like needle, body and orifices, are
 434 shown. The injector is a 5-hole, tapered (k-factor equal to 1.1) common rail injector. The injector is
 435 operating at an inlet pressure level of ~1800bar and the outlet pressure is ~50bar. The exact discharge
 436 pressure and needle lift are provided in Figure 8, estimated through simplified 1-D analysis⁴⁴.

437



438

439 Figure 8. A simple sketch of the examined injector and the operating conditions (needle lift and inlet pressure).

440

441 The cavitation number for the injector is significantly lower than the simplified throttle presented in
 442 section 3, due to the immense pressure difference:

$$443 \quad \sigma = \frac{p_{down} - p_{vap}}{p_{up} - p_{down}} = 0.028 \quad (13)$$

444 where p_{down} is the ambient/downstream pressure (50bar), p_{vap} is the vapor pressure (~1bar, based on

445 Diesel properties at 400K, see also^{44, 45}) and p_{up} is the upstream pressure of the injector (~1800bar).

446 The CN value of the injector case is ~36. The properties used for the simulation are based on

447 interpolation formulas from N. Kolev⁴⁵, derived at an average temperature of 400K, based on

448 preliminary 1D analysis including heating effects⁴⁶. Diesel density at saturation is $\rho_{L,sat} = 747.65\text{kg/m}^3$,

449 Diesel vapor pressure is ~1.1bar, Diesel bulk modulus is ~110MPa and Diesel liquid viscosity is given
450 by the following equation:

$$451 \quad \log_{10}(10^6 \mu_L / \rho) = 0.035065275 - 0.000234373 p / 10^5 \quad (14)$$

452 Diesel vapor density is 6.5kg/m³ based on the ideal gas equation at the saturation pressure and
453 temperature of 400K. Vapor viscosity is assumed constant and equal to 7.5μPa.s. Based on the
454 aforementioned properties and velocity/spatial scales the Reynolds number is estimated to be ~30000
455 inside the orifice hole at high lift operation.

456 The computational meshes used for the injector analysis are hexa-dominant block meshes with
457 structured and unstructured parts, with sufficient resolution depending on the assumptions of the
458 models used; the RANS mesh had ~300000-500000 cells for low-lift and high-lift operation, whereas
459 the LES mesh had a significantly higher resolution, starting at 10⁶ cells at low lifts and peaking at
460 1.75·10⁶ cells at high lifts. The LES resolution was based on the same guideline as in section 3, on the
461 Taylor scale. Based on the orifice diameter, the Taylor length scale is $\lambda_g \sim 7\mu\text{m}$, thus the grid sizing
462 selected was of equal size and additional refinement was employed near the walls. Also, high
463 resolution was maintained in critical areas of the injector, such as the needle/needle seat passage,
464 which is represented with at least 6cells for RANS and 10cells for LES at the minimum lift of 5μm
465 simulated. This number of cells is kept until a needle lift of ~40μm; beyond this point additional cell
466 layers are added (during opening) or removed (during closing) to the needle seat/needle passage. Both
467 cases solved only 1/5th of the whole injector tip, assuming only axial needle motion and symmetry
468 boundary conditions for RANS, or periodic boundary conditions for LES, at the sides of the
469 computational slice solved.

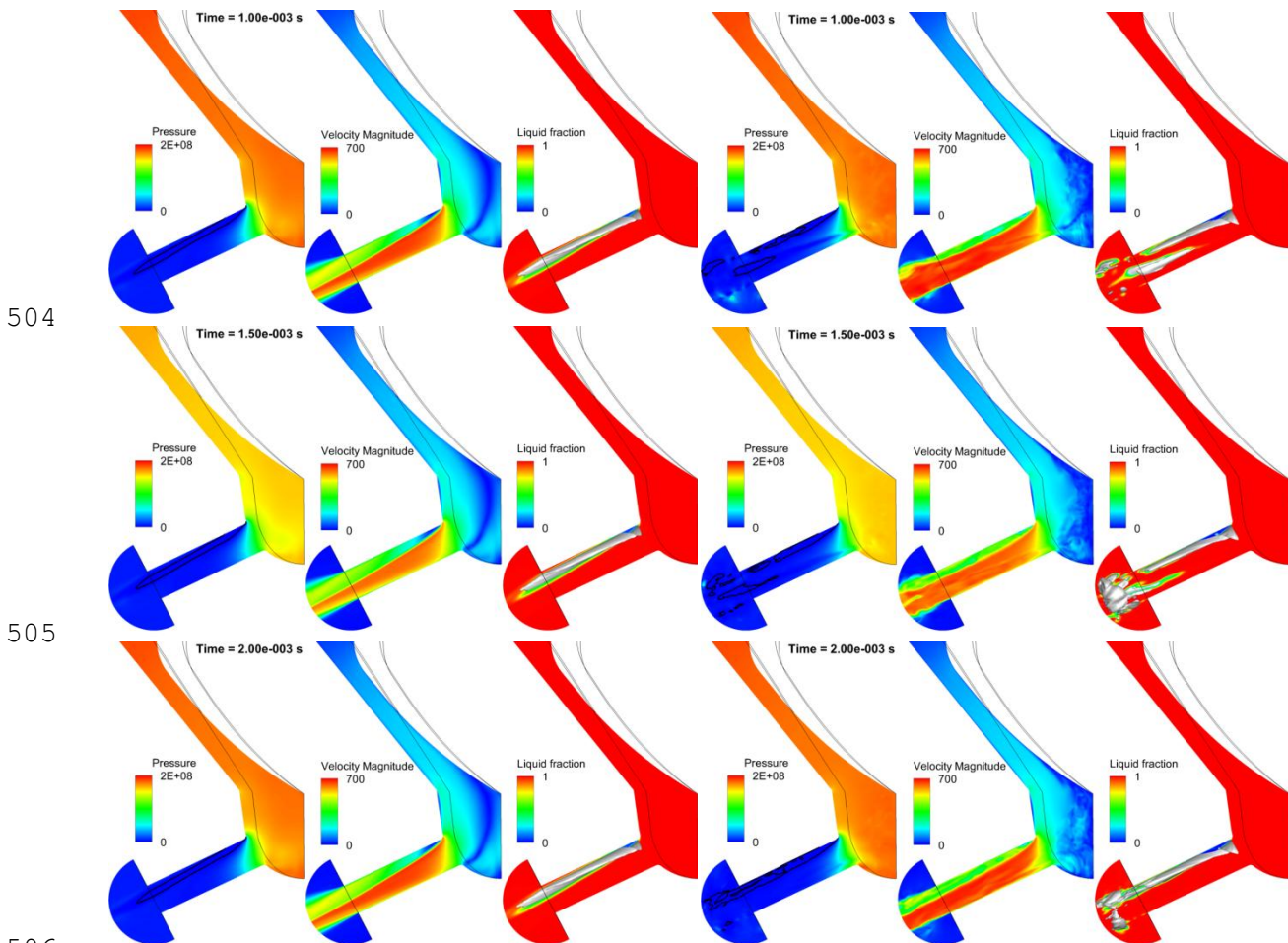
470 Several simulations have been performed with RANS models, including the RNG k-epsilon model
471 with Reboud correction, described in eq. 1 and the WALE LES model. The simulations to be
472 presented hereafter omit heating effects, mainly due to increased complexity and problematic behavior

473 of the polynomial relations at high pressures and temperatures. In RANS simulations the effect of
474 constant density and viscosity (set as the average based on the inlet and outlet conditions) as well as
475 varying density and viscosity was examined. For the LES case the modified ZGB model was used,
476 along with the Tait equation of state for the liquid. It is reminded that the modified ZGB model has
477 increased mass transfer rates for condensation and evaporation, in order to move the phase change
478 process closer to thermodynamic equilibrium. Standard cavitation models are prone to predicting
479 unrealistically high tension in the liquid, of the order of -300bar for Diesel injection cases, see also the
480 relevant work from Koukouvinis et al.^{44,47}. Increasing the mass transfer greatly reduces this tension, at
481 least by an order of magnitude, moving much closer to the saturation pressure. Moreover, high mass
482 transfer rates lead to replication of the Rayleigh collapse of vapor structures (for more information see
483 the Appendix B section), which is essential if one desires to capture pressure peaks from the cavity
484 collapses that could be linked to erosion. Unfortunately, the very time consuming nature of LES
485 simulations did not permit testing of different models, e.g. testing the barotropic model or constant
486 fuel properties. However the LES set-up discussed here has been found to predict a very similar
487 pressure peak pattern in comparison to relevant experiments, see ⁴⁴, which we consider, acts as a
488 validation.

489 The flow field results of the RANS simulations were very similar, irrespectively of using varying or
490 constant density/viscosity. While there is a notable increase in the mass flow rate of ~5%, when
491 varying density/viscosity is used, the macroscopic appearance of the flow field is the same. For
492 example, in Figure 9 the vapour fraction distribution inside the orifice hole is shown for the varying
493 density for several instances of the high lift operation, simulated with the RNG k-epsilon model with
494 Reboud correction. Despite some unsteadiness at the opening and closing phases on the injection,
495 during the high lift operation there is practically a steady attached cavity at the upper surface of the
496 orifice hole that maintains its size, topology and shape throughout the whole high lift operation. This
497 seems contradictory to real injector visualization studies, where cavity shedding and cavitating

498 vortices are found, see for example the work of Mitroglou et al.⁴⁸. Contrary to RANS, LES predicts a
499 much more unsteady vapor field, with an attached cavity at the upper hole surface that grows and
500 shrinks over time, periodic cavity shedding and occasional formation of cavitating vortices. Here it
501 should be mentioned that in cases of injectors with cylindrical holes (no tapering), unsteady flow was
502 predicted with the modified RANS model described above, as well as the LES model.

503



504

505

506

507 Figure 9. RANS (left) and LES (right) flow field at the midplane of the injector, for several instances at high lift
508 operation. Pressure (Pa), Velocity magnitude (m/s) and liquid volume fraction are shown at the slice; the thick
509 black line in the pressure slice denotes the region where pressure is lower the saturation and the grey isosurface
510 represents the surface at 0.5 vapour volume fraction. Note the significant instability of the flow field with
511 occasional appearance of cavitating vortices, as predicted with LES.

512

513

514

515

516

517 **6. Discussion**

518

519 From the results presented so far there are several important conclusions reached. First of all, it is
520 found that traditional RANS turbulence models may fail to predict a correct flow field in conjunction
521 with cavitation, both at low and high cavitation numbers. Indeed, the tight coupling of cavitation with
522 vortices, requires the accurate prediction of vortical structures in the flow, since those may contribute
523 to the generation and transport of cavitation formations. RANS models are not very well suited in this
524 role, since by their principle of operation, they do not aim to predict vortices, but rather a mean flow
525 path, compensating for unresolved structures with the addition of turbulent viscosity. While some
526 corrections to take into account turbulent fluctuations^{19, 20} and modifications to predict shedding exist
527^{13-15, 32}, their applicability seems case dependent and situational. These conclusions are supported by
528 other studies in literature as well²¹. Contrary to RANS/URANS models, Large Eddy Simulation
529 proven able to predict correctly both the averaged velocity profiles and the cavitation formation
530 mechanism at incipient cavitation (high σ , low CN), since it inherently aims to capture the larger
531 eddies that can contribute to cavitation development. Considering the injector results, at high intensity
532 cavitation (low σ , high CN), while modified RANS is capable of predicting cavitation, an unphysically
533 stable cavity is found, that contradicts experimental evidence. On the other hand, the examined LES
534 model predicts a proper cavity shedding and relevant instabilities; while in the injector case no
535 validation on the velocity field is available, recording of the pressure peaks due to vapor structure
536 collapse correlates well with the erosion pattern found in experiments, indicating a reasonable
537 reproduction of the vaporous flow structures.

538 In any case, from the results so far it seems that transient simulation is more successful in capturing
539 the velocity distribution, even for RANS. Of course it is easy to understand that unsteady simulations,
540 and even more LES with its special grid requirements, are rather intensive to resolve. However, given
541 the observed deficiency of standard RANS models to predict the correct flow in many cases, it seems

542 that LES/DES or similar scale resolving methods are essential for the proper flow representation.
543 Alternatively, it could be the case that there is a need for the development of new turbulence models
544 that can correlate turbulent characteristics with cavitation in a better way than existing models. In any
545 case, one should not forget that many turbulence models have been developed in the past, but still each
546 of them has limited applicability. In other words such an effort might lead to another situational RANS
547 model that performs well in some cases and bad in others; after all, the need to resort in scale resolving
548 simulations more and more, even in industrial level, could mean that the level of accuracy required
549 nowadays justifies the use of more computationally expensive models such as LES. Undeniably,
550 RANS models can (and will) still play a role in industrial numerical simulations, since they can offer a
551 solution very fast, being ideal for e.g. design/optimization studies.

552 Regarding the influence of the cavitation model, it seems that at low intensity cavitation it did not play
553 a significant role in the average flow pattern. While to reach a final conclusion a quantitative
554 comparison of vapor fraction distribution is required, relevant data are not available and in general are
555 difficult to obtain. This forces to resort to qualitative comparisons of indicative cavitation instances,
556 which clearly show a cavitation shedding mechanism. Also, from the aforementioned results, it is
557 visible that the increased mass transfer rates of the modified ZGB model result to moving closer to
558 thermodynamic equilibrium and reduction of the magnitude of negative pressures. Whereas in the
559 enlarged nozzle case this does not seem to have a pronounced effect to the macroscopic characteristics
560 of the flow field, this is not the case at high intensity cavitation cases, like the flow inside the real
561 injector. As discussed in the relevant section, the standard formulation of commonly used cavitation
562 models lead to unrealistically high liquid tension. Thus in such cases it is essential to modify the
563 cavitation model accordingly, in order to move closer to thermodynamic equilibrium. Unfortunately
564 how close to or far from thermodynamic equilibrium each case is, is not known a priori. For water
565 there is some evidence that cavitation behaves as a thermodynamic equilibrium process, see the
566 interesting work of Washio³⁹. It is our opinion that more fundamental work is required on the

567 thermodynamics of fluids, for the understanding of meta-stability that affects cavitation and other
568 effects such as flashing.

569

570 **7. Conclusion**

571

572 This paper evaluates the predictive capability of 2-equation and 7-equation RANS models to simulate
573 incipient cavitation in an enlarged rectangular step nozzle and developed cavitation in an actual Diesel
574 injector, and compares the results with WALE LES model predictions. The LES model is also used to
575 further investigate the performance of barotropic and 2-phase mass transfer cavitation models.

576 Both cases show the situational applicability of RANS model for predicting cavitation. For the
577 enlarged step nozzle, all the RANS models used, i.e. the Realizable $k-\epsilon$, SST $k-\omega$ and RSM model
578 failed to predict pressures below the saturation pressure. RANS is a useful tool for many cavitation
579 problems as seen in the literature, but its limited capability has also been reported for cases with small
580 amounts of cavitation²¹. For problems such as incipient cavitation in a nozzle where the pressure drop
581 from inlet to outlet is low, small vortices are formed that act as nucleation sites for bubbles. In order to
582 capture these flow structures, more rigorous turbulence models such as LES are required. The average
583 minimum pressure predicted by the barotropic and the non-equilibrium cavitation models is above the
584 saturation pressure of water. This result further justifies the minimum pressure predicted by RANS
585 models, which is above saturation pressure. Furthermore, changing the cavitation model did not
586 significantly affect the streamwise velocity outside the cavitation region. The predicted shape of the
587 cavity was in agreement with experimental images, however quantitative measurements inside the
588 vapour volume is required to judge the accuracy of the calculated cavitation.

589 At high cavitation intensity RANS models may predict cavitation, but the predicted structure may be
590 unrealistically stable, especially in cases of hole tapering where orifice turbulence is suppressed. The
591 LES model tested was found able to reproduce an unsteady flow field, even in the cases of tapered

592 holes, but comes with a very high price, since the associated computational cost is significantly higher
593 than that of RANS. Just for reference, an LES simulation may require 20x the time of an URANS
594 simulation and maybe more than 1000x the time needed for a steady state RANS simulation.
595 Potentially, the future lies on scale adaptive models and RANS/LES hybrids, such as Detached Eddy
596 Simulation.

597

598 **Acknowledgements**

599 The research leading to these results has received funding from the People Programme (IAPP Marie
600 Curie Actions) of the European Union's Seventh Framework Programme FP7/2007-2013/ under REA
601 grant agreement n. 324313. We have also to thank Caterpillar Inc. for providing the injector
602 geometries, operating conditions and experimental results regarding erosion.

603

604 **Disclaimer**

605

606 CAT, CATERPILLAR, their respective logos, “Caterpillar Yellow,” the “Power Edge” trade dress as
607 well as corporate and product identity used herein, are trademarks of Caterpillar and may not be used
608 without permission. ©2015 Caterpillar All Rights Reserved.

609

610 **Nomenclature**

611

a	Vapor fraction (-)
ρ	Density (kg/m ³)
μ_t	Turbulent viscosity (Pa.s)
ν	Kinematic viscosity (m ² /s)
k	Turbulent kinetic energy (m ² /s ²)
ε	Turbulent dissipation (m ² /s ³)

ω	Specific dissipation rate (1/s)
S_{ij}	Strain rate tensor, ij component (1/s)
c	Speed of sound (m/s)
p	Pressure (Pa)
B	Bulk modulus (Pa)
\mathbf{u}	Velocity vector field (m/s)
R_e, R_c	Evaporation and condensation source terms for the 2-phase model (kg/s/m ³)
σ	Cavitation number (-)
CN	Alternative definition of cavitation number, equal to $1/\sigma$ (-)
η	Kolmogorov length scale (m)
τ_η	Kolmogorov temporal scale (m)
λ_g	Taylor length scale (m)
u^*	Friction velocity (m/s)
δ_s	Viscous sublayer thickness (m)

612

613 **Appendix A: Derivation of the mixture part equation of state.**

614

615 Starting with the definition of the speed of sound:

616
$$c^2 = \left(\frac{\partial p}{\partial \rho} \right)_s \quad (15)$$

617 and the Wallis speed of sound for bubbly mixtures:

618
$$\frac{1}{c_m^2 \rho_m} = \frac{a_l}{c_l^2 \rho_l} + \frac{a_v}{c_v^2 \rho_v} \quad (16)$$

619 one may formulate pressure as:

620
$$p = \int c^2 d\rho + p_{ref} \Rightarrow$$

621
$$p = \int \left[\rho \left(\frac{1-a_v}{c_l^2 \rho_l} + \frac{a_v}{c_v^2 \rho_v} \right) \right]^{-1} d\rho + p_{ref} \quad (17)$$

622 where the vapour fraction is a function of density:

$$623 \quad a_v = \frac{\rho - \rho_v}{\rho_l - \rho_v} \quad (18)$$

624 The result of the integration in eq. 17, considering also eq. 18 is shown below:

$$625 \quad p = \frac{c_v c_l (\rho_v - \rho_l) \rho_v \rho_l}{\rho_v^2 c_v^2 - \rho_l^2 c_l^2} \left[\ln(\rho) - \ln \left[c_v^2 \rho_v (\rho - \rho_v) + c_l^2 \rho_l (\rho_l - \rho) \right] \right] + p_{ref} \quad (19)$$

626 Based on logarithm properties, eq. 19 may be written as:

$$627 \quad p = \frac{c_v c_l (\rho_v - \rho_l) \rho_v \rho_l}{\rho_v^2 c_v^2 - \rho_l^2 c_l^2} \ln \left(\frac{\rho}{c_v^2 \rho_v (\rho - \rho_v) + c_l^2 \rho_l (\rho_l - \rho)} \right) + p_{ref} \quad (20)$$

628 which is the mixture relation in the HEM EOS (eq. 6), valid only when density is between liquid and
629 vapour saturation densities, i.e. $\rho_l \geq \rho > \rho_v$.

630

631 **Appendix B: Comparison between the 2-phase and barotropic models in fundamental cases.**

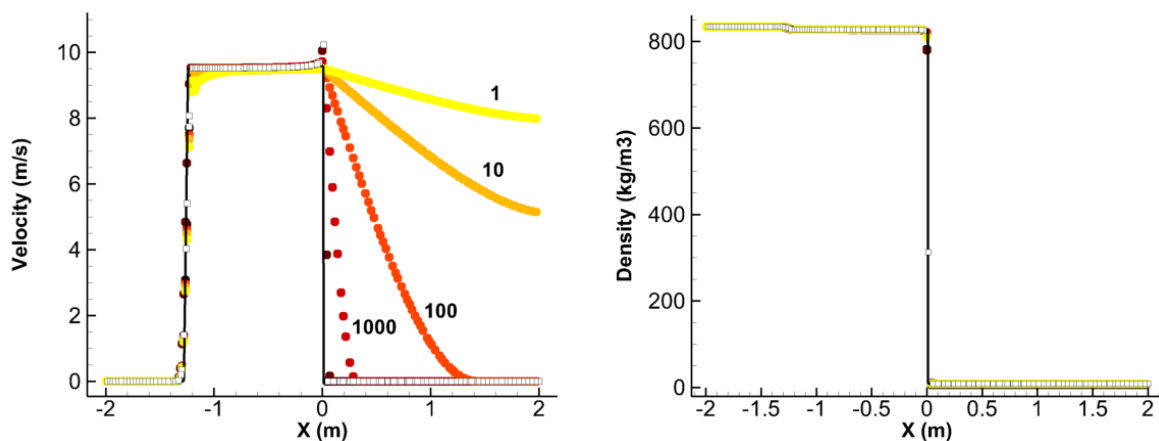
632

633 In this section a comparison between the 2-phase mass transfer and barotropic models is discussed in a
634 more fundamental basis, in order to show clearly the effect of their assumptions. Moreover, the
635 influence of the mass transfer rate is examined.

636 A first case examined is a shock tube case. The shock tube is a fundamental test of compressible flows
637 where a simple 1D flow is considered. There are two distinct states, the left state (L, for $x < 0m$) and
638 right state (R, for $x \geq 0m$), separated by an initial discontinuity at $x = 0m$. The two states that are
639 examined here are pure diesel liquid as the left state, at a pressure of 100bar, and a liquid/vapour
640 mixture, at saturation pressure ($\sim 892Pa$) and 90% vapour fraction. The thermodynamic model for the
641 materials is either the 2-phase mixture or barotropic HEM, as discussed in sections 2.2 and 2.3. An
642 exact solution of the problem for the barotropic HEM model may be derived using the Rankine-
643 Hugoniot conditions and Riemann invariants, see the book of Toro⁴⁹. As will be shown later, the exact
644 solution can serve as an asymptotic solution for the 2-phase mass transfer model as well, when the

645 mass transfer is high enough. It has to be highlighted that the solution of the Riemann problem for
646 such equations of state is not trivial; the interested reader is addressed to the recent work of
647 Koukouvinis et al.⁵⁰ for more information about the exact solver. The numerical solution is obtained
648 using 1000 cells in the x direction.

649 In Figure 10, a comparison between the numerical and exact solutions between the models is shown at
650 time of 1ms. As it is visible, the exact solution and the barotropic HEM solution match perfectly,
651 which also acts as a validation of the described methodology in section 2.3. The 2-phase solution is
652 greatly dependent on the mass transfer rate, see the source term of eq. 7. For high mass transfer rates
653 (which are represented by the dark red cycles in Figure 10), the solution converges to the exact
654 barotropic HEM solution. This is reasonable, because the mass transfer term affects the mixture speed
655 of sound; increasing the mass transfer results to a decreased mixture speed of sound, see also Franc¹.
656 On the other hand, when the mass transfer term is low, then the mixture speed of sound increases,
657 leading a more diffused profile in the velocity distribution (see the light red, orange and yellow circles
658 in Figure 10). The same effect is found in density field as well, but it is much less observable. Each 2-
659 phase mixture solution has an increase in the mass transfer rate by one order of magnitude, i.e. the
660 dark red cycles solution has a 10^4 higher mass transfer rate than the light yellow reference solution.



662 Figure 10. Shock tube case, comparison between various models at $t = 1\text{ms}$. Continuous line is the exact
663 solution, white filled squares are the numerical barotropic HEM solution and coloured cycles are the 2-phase
664 mass transfer solution. The colour of the cycles represents the magnitude of the mass transfer term, which is
665 mentioned in text also near the respective line: yellow ($1\times$ multiplier for the reference mass transfer) for low
666 mass transfer rates to dark red ($10^4\times$ multiplier for the reference mass transfer) for high mass transfer rates.

667

668 Another test case, commonly used in cavitating flows, is the Rayleigh collapse. A sphere of vapour is
669 subjected to compression due to the influence of the surrounding high pressure liquid. This case has an
670 exact and well known solution, where the radius of the bubble reduces in an accelerating manner, with
671 bubble wall velocity tending to infinity, see e.g. Franc¹. In that case, the bubble collapse velocity,
672 dR/dt , is given by the following relation:

$$673 \quad \frac{dR}{dt} = -\sqrt{\frac{2}{3} \frac{p_\infty - p_v}{\rho} \left[\left(\frac{R_0}{R} \right)^3 - 1 \right]} \quad (21)$$

674 where:

675 - p_∞ is the pressure at the farfield

676 - p_v is the vapour pressure

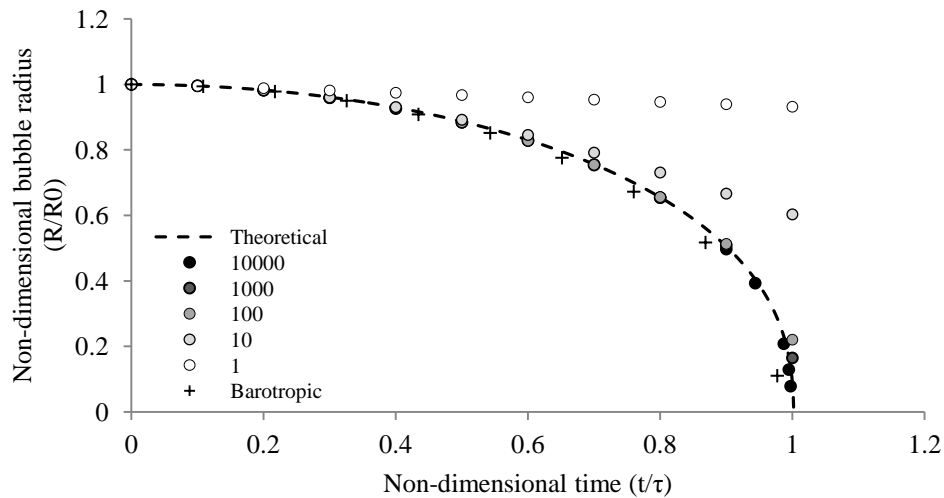
677 - ρ is the liquid density

678 - R_0 is the initial bubble radius and R is the current bubble radius

679 By integrating the bubble wall motion, it is possible to find the bubble collapse time:

$$680 \quad \tau \cong 0.915 R_0 \sqrt{\frac{\rho}{p_\infty - p_v}} \quad (22)$$

681 Here, the collapse of water vapour bubble at pressure $p_v = 2339\text{Pa}$ and initial radius $R_0=10\mu\text{m}$ is
682 examined. The case is resolved as 2D axis-symmetric simulation, with a 60000 cells. Indicative results
683 are shown in Figure 11, where the theoretical evolution of the bubble radius is compared with the
684 numerical solutions. In order to have a fair comparison, both models were simulated with a timestep of
685 1ns. For the 2-phase model, it is clear that only at a high mass transfer rate the proper behaviour of the
686 Rayleigh collapse is replicated. The barotropic HEM model predicts a bubble collapse very close to
687 the theoretical. The mismatch is found to be due to the timestep; the higher the convective Courant
688 number, the more diffuse the bubble interface becomes with the HEM model. Significantly reducing
689 the timestep greatly improves the agreement with the theoretical solution.



690

691 Figure 11. Rayleigh collapse test case, comparison of the bubble radius evolution for various models. The dashed
 692 line shows the exact solution, crosses the barotropic model HEM solution, whereas circles the 2-phase model
 693 solution (the mass transfer is higher for dark circles and lower for whiter circles, a reference multiplier is given
 694 in legend).
 695

696 From the discussed examples, the conclusion is that the 2-phase mass transfer model and barotropic
 697 HEM model are equivalent for high mass transfer rates of the latter. Other practical comparisons of the
 698 two models, in e.g. throttle flows, may be found in a recent work of Koukouvinis et al.⁴⁷, supporting
 699 the aforementioned conclusion.

700

701 **References**

702

703 1. Franc J-P and Michel J-M. *Fundamentals of Cavitation*. Kluwer Academic Publishers, 2005.
 704 2. Afzal H, Arcoumanis C, Gavaises M and Kampanis N. Internal flow in diesel injector
 705 nozzles: modelling and experiments. *IMechE Paper S*. 1999; 492: 25-44.
 706 3. Andriotis A, Gavaises M and Arcoumanis C. Vortex flow and cavitation in diesel injector
 707 nozzles. *Journal of Fluid Mechanics*. 2008; 610: 195-215.
 708 4. Arndt RE. Cavitation in vortical flows. *Annual Review of Fluid Mechanics*. 2002; 34: 143-
 709 75.

- 710 5. Pozrikidis C. Fluid dynamics: theory, computation, and numerical simulation. Springer
711 Science & Business Media, 2009.
- 712 6. Laberteaux K and Ceccio S. Partial cavity flows. Part 1. Cavities forming on models without
713 spanwise variation. *Journal of Fluid Mechanics*. 2001; 431: 1-41.
- 714 7. Bin J, Luo X-w, Peng X-x and Wu Y-l. Three-dimensional large eddy simulation and
715 vorticity analysis of unsteady cavitating flow around a twisted hydrofoil. *Journal of Hydrodynamics,*
716 *Ser B*. 2013; 25: 510-9.
- 717 8. Chahine G and Genoux PF. Collapse of a cavitating vortex ring. *Journal of fluids*
718 *engineering*. 1983; 105: 400-5.
- 719 9. Simpson RL. Turbulent boundary-layer separation. *Annual Review of Fluid Mechanics*.
720 1989; 21: 205-32.
- 721 10. Iyer CO and Ceccio SL. The influence of developed cavitation on the flow of a turbulent
722 shear layer *Physics of Fluids* 2002; 14: 3414-31.
- 723 11. Okabayashi K and Kajishima T. Investigation of turbulent modulation by cavitation for
724 subgrid-scale modeling in LES CAV2009. Ann Arbor, Michigan, USA2009.
- 725 12. Dular M and Delgosha OC. Numerical modelling of cavitation erosion. *International*
726 *Journal for Numerical Methods in Fluids*. 2009; 61: 1388–410.
- 727 13. O. Coutier-Delgosha, J. L. Reboud and Delannoy Y. Numerical simulation of the unsteady
728 behaviour of cavitating flows. *International Journal for Numerical Methods in Fluids*. 2003; 42: 527-
729 48.
- 730 14. O. Coutier-Delgosha, J. L. Reboud and Fortes-Patella R. Evaluation of the Turbulence
731 Model Influence on the Numerical Simulations of Unsteady Cavitation. *Journal of Fluids*
732 *Engineering*. 2003; 125: 38-45.
- 733 15. Reboud J-L, Stutz B and Coutier O. Two-phase flow structure of cavitation: experiment and
734 modelling of unsteady effects. *Third International Symposium on Cavitation*. Grenoble, France1998.

- 735 16. Decaix J and Goncalvès E. Compressible effects modeling in turbulent cavitating flows.
736 *European Journal of Mechanics - B/Fluids*. 2013; 39: 11-31.
- 737 17. Wu J, Wang G and Shyy W. Time-dependent turbulent cavitating flow computations with
738 interfacial transport and filter-based models. *International Journal for Numerical Methods in Fluids*.
739 2005; 49: 739-61.
- 740 18. Decaix J and Goncalvès E. Time-dependent simulation of cavitating flow with $k-\ell$
741 turbulence models. *International Journal for Numerical Methods in Fluids*. 2012; 68: 1053-72.
- 742 19. Giannadakis E. Modelling of Cavitation in Automotive Fuel Injector Nozzles. *Department of*
743 *Mechanical Engineering*. University of London, 2005, p. 431.
- 744 20. Singhal AK, Athavale M, Li H and Jiang Y. Mathematical Basis and Validation of the Full
745 Cavitation Model *Journal of Fluids Engineering*. 2002; 124: 617-24.
- 746 21. Edelbauer W, Struel J and Morozov A. Large Eddy Simulation of cavitating throttle flow.
747 *SimHydro 2014:Modelling of rapid transitory flows*. Sophia Antipolis2014.
- 748 22. Örley F, Hickel S, Schmidt SJ and Adams NA. LES of cavitating flow inside a Diesel
749 injector including dynamic needle movement. *Journal of Physics: Conference Series*. 2015; 656.
- 750 23. Sou A, Bicer B and Tomiyama A. Numerical simulation of incipient cavitation flow in a
751 nozzle of fuel injector. *Computers & Fluids* 2014; 103: 42 - 48.
- 752 24. Ducros F, Nicoud F and Poinot T. Subgrid-scale modeling based on the square of the
753 velocity gradient tensor flow. *Turbulence and Combustion*. 1999; 62: 183-200.
- 754 25. Schnerr GH and Sauer J. Physical and numerical modelling of unsteady cavitation dynamics.
755 *Proceedings ICMF-2001 – 4th International Conference on Multiphase Flow*. New Orleans,
756 USA2001.
- 757 26. Zwart PJ, Gerber AG and Belamri T. A two-phase flow model for predicting cavitation
758 dynamics *5th International Conference on Multiphase Flow* Yokohama, Japan2004.
- 759 27. Schmidt D. Cavitation in Diesel Fuel Injector Nozzles. University of Wisconsin - Madison,
760 1997.

- 761 28. Versteeg H and Malalsekera W. An Introduction to Computational Fluid Dynamics: The
762 Finite Volume Method. Prentice Hall, 2007.
- 763 29. Pope S. *Turbulent Flows*. Cambridge University Press, 2000.
- 764 30. Wilcox D. *Turbulence Modeling for CFD*. D C W Industries, 2006.
- 765 31. Launder BE. Second-moment closure and its use in modelling turbulent industrial flows.
766 *International Journal for Numerical Methods in Fluids*. 1989; 9: 963-85.
- 767 32. Delgosha OC, Patella F and Reboud J-L. Simulation of unsteady cavitation with a two-
768 equation turbulence model including compressibility effects. *Journal of Turbulence*. 2002; 3.
- 769 33. Sarkar S and Lakshmanan B. Application of a Reynolds stress turbulence model to the
770 compressible shear layer. *AIAA Journal*. 1991; 29: 743-9.
- 771 34. Brennen C. *Cavitation and Bubble Dynamics*. Oxford University Press, 1995.
- 772 35. Koop AH. Numerical Simulation of Unsteady Three-Dimensional Sheet Cavitation.
773 University of Twente, 2008.
- 774 36. Ivings MJ, Causon DM and Toro EF. On Riemann solvers for compressible liquids.
775 *International Numerical Methods for Fluids*. 1998; 28: 395-418.
- 776 37. Holmgren M. X-steam v2.6, <http://xsteam.sourceforge.net/>.
- 777 38. Caupin F and Stroock AD. The Stability Limit and other Open Questions on Water at
778 Negative Pressure. *Liquid Polymorphism*. 2013; 152.
- 779 39. Washio S. Recent Developments in Cavitation Mechanisms: Cavitation inception in
780 separating water flows. *A Guide for Scientists and Engineers*. Elsevier, 2014, p. 133-57.
- 781 40. Addad Y, Gaitonde U, Laurence D and Rolfo S. Optimal Unstructured Meshing for Large
782 Eddy Simulations. In: Meyers J, Geurts B and Sagaut P, (eds.). *Quality and Reliability of Large-Eddy*
783 *Simulations*. Netherlands: Springer, 2008.
- 784 41. Bogey C and Bailly C. Influence of Reynolds number and grid resolution on large-eddy
785 simulations of self-similar jets based on relaxation filtering. In: Salvetti MV, Geurts B, Meyers J and
786 Sagaut P, (eds.). *Quality and Reliability of Large-Eddy Simulations II*. Netherlands: Springer, 2011.

- 787 42. Sagaut P. Large Eddy Simulation for Incompressible Flows: An Introduction. Berlin:
788 Springer-Verlag 2006.
- 789 43. Egler W, Giersch JR, Boecking F, et al. Fuel Injection Systems. In: Mollenhauer K and
790 Tschöke H, (eds.). *Handbook of Diesel Engines*. 1 ed.: Springer-Verlag Berlin Heidelberg, 2010, p.
791 127-74.
- 792 44. Koukouvinis P, Gavaises M, Li J and Wang L. Large Eddy Simulation of Diesel injector
793 including cavitation effects and correlation to erosion damage. *Fuel*. 2016; 175: 26-39.
- 794 45. Kolev N. *Multiphase Flow Dynamics 3*. Springer Berlin Heidelberg, 2007.
- 795 46. Strotos G, Koukouvinis P, Theodorakakos A, Gavaises M and Bergeles G. Transient heating
796 effects in high pressure Diesel injector nozzles. *International Journal of Heat and Fluid Flow*. 2015;
797 51: 257-67.
- 798 47. Koukouvinis P and Gavaises M. Simulation of throttle flow with two phase and single phase
799 homogenous equilibrium model. *Journal of Physics: Conference Series*. 2015; 656: 012086.
- 800 48. Mitroglou N, McLorn M, Gavaises M, Soteriou C and Winterbourne M. Instantaneous and
801 ensemble average cavitation structures in Diesel micro-channel flow orifices. *Fuel*. 2014; 116: 736-42.
- 802 49. Toro E. Riemann Solvers and Numerical Methods for Fluid Dynamics: A Practical
803 Introduction. Springer-Verlag Berlin Heidelberg, 2009.
- 804 50. Koukouvinis P, Gavaises M, Georgoulas A and Marengo M. Compressible simulations of
805 bubble dynamics with central-upwind schemes. *International Journal of Computational Fluid
806 Dynamics*. 2016.
- 807
- 808